Advanced Energy Materials

ADVANCED ENERGY MATERIALS
www.advenergymat.de

RESEARCH ARTICLE OPEN ACCESS

Molecular Bottom-Up Design of Single-Site Copper-Palladium Catalysts for Selective Glycerol Electro-Oxidation

Soressa Abera Chala[1] | Ekemena O. Oseghe[1] | Keseven Lakshmanan[2] | Marcel Langer[1] | Katharina Potemkin[1] | Paul Heim[1] | Rongji Liu[1] | Tobias Rios Studer[1] | Meng-Che Tsai[3] | Kecheng Cao[4] | Chun-Chi Chang[2] | Chia-Yu Chang[2] | Kevin Sowa[1] | Elnaz Ebrahimi[1] | Sarra Rahali[1] | Simon T. Clausing[1] | Sina Sadigh Akbari[1] | Joachim Bansmann[5] | Bing Joe Hwang[2,6] | Carsten Streb[1]

[1]Department of Chemistry, Johannes Gutenberg University Mainz, Mainz, Germany | [2]Sustainable Electrochemical Energy Development (SEED) Center, National Taiwan University of Science and Technology, Taipei, Taiwan | [3]Department of Greenergy, National University of Tainan, Tainan, Taiwan | [4]School of Physical Science and Technology & Shanghai Key Laboratory of High-resolution Electron Microscopy, Shanghai Tech University, Shanghai, China | [5]Institute for Surface Chemistry and Catalysis, Ulm University, Ulm, Germany | [6]National Synchrotron Radiation Research Center (NSRRC), Hsinchu, Taiwan

Correspondence: Soressa Abera Chala (soressa-abera.chala@uni-mainz.de) | Bing Joe Hwang (bjh@mail.ntust.edu.tw) | Carsten Streb (carsten.streb@uni-mainz.de)

Received: 9 August 2025 | **Revised:** 19 December 2025 | **Accepted:** 29 December 2025

Keywords: electrocatalysis| glycerol oxidation reaction| phthalocyanine| single-site catalyst| X-ray absorption spectroscopy

ABSTRACT

Hybrid water electrolysis is a promising route to generate hydrogen while replacing the challenging and wasteful oxygen evolution reaction (OER) with economically viable alternatives such as the selective glycerol oxidation reaction (GOR). To date, the development of highly active and selective GOR electrocatalysts remains a major challenge because the simultaneous control of reactivity, selectivity, and stability is difficult. Herein, we report a bimetallic Cu-Pd single-site catalyst (SSC) for the selective and efficient electrooxidation of glycerol. The catalyst features single-site copper and palladium atoms in CuN_4/PdN_4 moieties. The catalyst shows high GOR performance with a Faradaic efficiency (FE) for formate of 83% and C3 products (lactate, glycolate, glycerate) of 16% at 1.0 V vs the reversible hydrogen electrode (RHE), as well as long-term stability (144 h at $j = 50$ mA cm^{-2}). Mechanistic studies combining DFT and *operando* spectroscopy revealed that Pd sites facilitate the adsorption of hydroxyl (C-OH) species which prevents C-C bond cleavage and thus the formation of catalyst poisons such as CO or CO_3^{2-}. This work sheds light on the adsorption modulation mechanism of a single-site catalyst and provides a promising electrocatalytic system for the production of value-added C1 and C3 products in aqueous solution.

1 | Introduction

Electrochemical splitting of water into oxygen and hydrogen is the backbone for carbon-neutral, sustainable energy scenarios [1, 2]. In water splitting, hydrogen is desirable as a valuable secondary energy carrier, while oxygen is released as a waste product. However, the overall process efficiency is limited by the anodic oxygen evolution reaction (OER), which suffers from sluggish reaction kinetics and harsh oxidative conditions, leading to significant energy loss and catalyst degradation [3, 4]. Thus, replacing the challenging and undesired OER with a productive anodic reaction could be a major boost for the development of a hydrogen economy. The concept of hybrid water electrolysis has received significant interest in recent years, with various anodic oxidations being used to replace the OER.

The selective glycerol oxidation reaction (GOR) has emerged as a promising OER alternative owing to its lower theoretical oxidation potential (~0.0 V vs. the reversible hydrogen electrode, RHE), which significantly reduces the overall energy input required [5–7]. Glycerol is an attractive biogenic feedstock available on a large scale at low cost, as it is a low-value byproduct of biodiesel production. Its valorization by GOR can contribute to a circular economy while providing value-added C1-C3 glycerol oxidation products, such as formate, glycolate, glycerate, and lactate, which are currently produced in expensive and unsustainable processes [5–9].

Noble metal-based nanostructured electrocatalysts have been extensively studied for the GOR, demonstrating high activity and selectivity [10]. However, their practical application is limited by their high cost and scarcity. In response, efforts have been made to explore noble-metal-free transition-metal-based catalysts, which often fall short of achieving the necessary combination of high performance, stability, and selectivity. A promising alternative is to explore the potential of noble metal containing single-site catalysts (SSCs) as a technologically viable alternative to bulk noble metals [11, 12]. The successful fabrication and deployment of these SSCs would result in an ideal atom utilization and reduced usage of noble metals [13]. SSCs have garnered significant attention in electrocatalysis due to their unique atomic dispersion, high catalytic activity, and exceptional stability, making them a potential game-changer in the development of efficient electrocatalysts [14, 15]. While several SSCs based on non-noble (e.g., Bi and Cu) [16, 17] and noble metals (e.g., Pt) [18] have been explored for the electrochemical oxidation of glycerol; however, to the best of our knowledge, palladium (Pd)-based SSCs have not been studied, despite its favorable electrocatalytic properties and relative abundance [19]. Relative to Pt, Pd has a higher oxidation potential, which ensures excellent stability over longer electrochemical cycles [20] making Pd-based SSCs a potential candidate for GOR. Therefore, a well-designed protocol for the preparation of Pd-containing dual-atom SSCs is necessary.

As an extension of monometallic SSCs, bimetallic SSCs with high metal contents and flexible active sites can trigger the synergistic effects of neighboring atoms and give them new catalytic properties [21, 22]. Bimetallic SSCs not only inherit the advantages of monometallic SSCs, but also improve the intrinsic catalytic activity of the active sites through the synergistic interaction between the two metal atoms, improving activity, selectivity, and stability beyond what is achievable with monometallic SSCs, especially in electrocatalysis processes involving multiple reaction pathways and reaction sites [23–26]. However, the design and synthesis of bimetallic SSCs with isolated reactive sites remain challenging, particularly for complex reactions such as GOR. Therefore, a well-designed protocol and synthesis strategy is required to develop highly efficient bimetallic SSCs with abundant metal content and to elucidate the associated catalytic reaction mechanism.

Recent advances in the electrochemical restructuring of molecular catalysts, such as copper(II) phthalocyanine (CuPc), have demonstrated their ability to reversibly transform into single-site Cu clusters embedded within nitrogen-defective carbon frameworks [27–30]. This dynamic restructuring opens a promising avenue for the incorporation of secondary metal cations into the vacant coordination sites, enabling the rational design of bimetallic SSCs with tunable electronic environments and enhanced catalytic functionality. Yet, this promising avenue has not been explored in the context of SSC preparation and application.

Here, we report the electrochemical synthesis of a Cu-Pd dual-atom SSC (hereafter **CuPd**) derived from CuPc, designed for efficient and selective glycerol oxidation. The catalyst exhibits high activity and selectivity toward C1-C3 products, along with excellent stability. Mechanistic studies reveal the synergistic interplay between Cu and Pd sites, providing insights into the enhanced performance. This work introduces a new strategy for the design of dual-atom SSCs and expands their application to energy-efficient biomass upgrading.

2 | Results

Figure 1 schematically outlines the synthesis of bimetallic **CuPd** SSCs from a molecular complex of CuPc using an electrochemical reduction method. This approach is inspired by earlier studies, where CuPc was used as a catalyst for CO_2 reduction and structurally transformed from atomically dispersed Cu sites to Cu clusters during the reductive potential [27]. Here, this approach was expanded to electrochemically reduce CuPc under neutral conditions to give metallic copper clusters and a macrocyclic structure of phthalocyanine ligand with vacant metal binding sites, where Pd^{2+} ions were subsequently introduced and anchored to obtain bimetallic **CuPd** SSCs. Benefitting from the high metal content of CuPc and the restructuring properties of Cu sites, a high metal loading of bimetallic **CuPd** SSCs with neighboring Cu clusters and CuN_4/PdN_4 moieties was obtained after applying a constant reduction potential (−1.2 V vs. RHE) to the CuPc electrode for 3 h and immersed in a $PdCl_2$ solution. The samples were used for catalytic applications without further treatment.

To optimize the synthesis process, four **CuPd** samples were prepared and labelled CuPd-x, where x = 0.5, 1 (hereafter: **CuPd**), 2, and 3 h represents the duration for which the reduced CuPc electrode was immersed in the $PdCl_2$ solution. For comparison, we also prepared two reference electrodes; one contained only reduced CuPc (**Ref-Cu**), while the other contained non-reduced CuPc and Pd (obtained by immersion in a $PdCl_2$ solution, **Ref-CuPd**). The Cu and Pd metal contents of the electrodes were analyzed using inductively coupled plasma optical emission spectrometry (ICP-OES) and are listed in Table S1. The Cu and Pd content of **CuPd** SSCs was determined to be 8.62 and 9.27 wt.%, respectively. As a control, we also analyzed the Pd loading of the **Ref-CuPd** sample and found a Pd content of 1.56 wt.%, indicating minor physiosorbed Pd species on the unreduced CuPc electrode. This observation shows that the electrochemical reduction of the CuPc electrode generates abundant metal anchoring sites in the CuPc structure where Pd ions are anchored, thus enabling the formation of atomically dispersed Pd sites in **CuPd** SSCs.

The morphology and structure of the catalysts were analyzed by scanning electron microscopy (SEM), transmission electron microscopy (TEM) and high-resolution TEM. The SEM images show the morphological changes of CuPc from the original submicron-sized particles (Figure 2a) to the final nanostructured particles after the incorporation of Pd^{2+} ions in **CuPd** SSCs

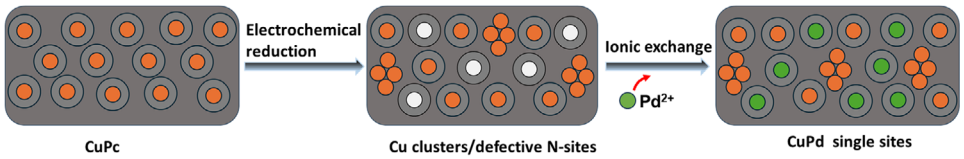

FIGURE 1 | (a) Schematic representation of the synthesis of bimetallic **CuPd** SSCs through the electrochemical reduction of CuPc.

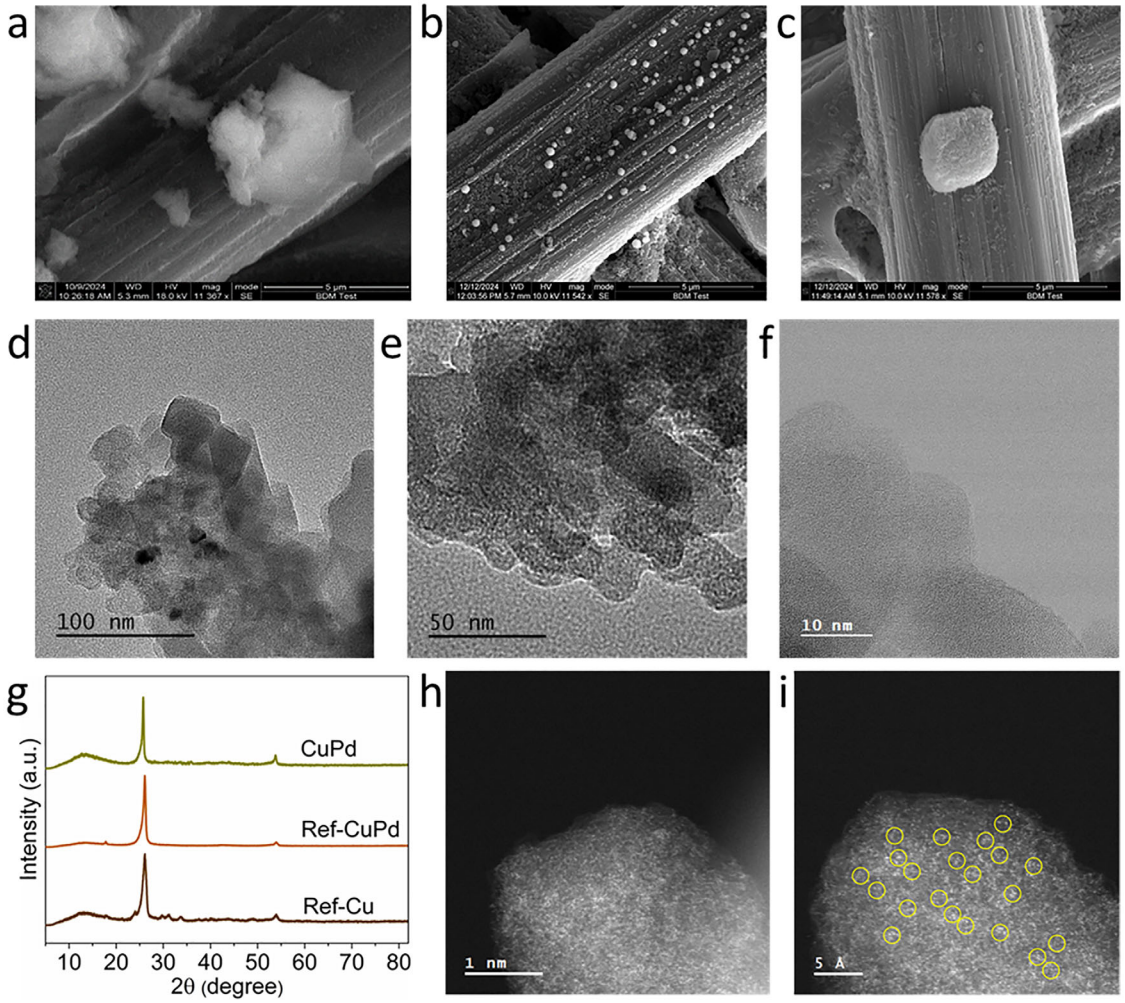

FIGURE 2 | SEM images of (a) CuPc, (b) **CuPd** SSCs, (c) **Ref-Cu**. (d-f) TEM images of **CuPd** SSCs, and (g) XRD patterns of **Ref-Cu**, **Ref-CuPd** and **CuPd** SSCs. (h, i) Aberration-corrected HAADF-STEM images of the **CuPd** SSCs at different magnifications, showing individual Cu/Pd dual-sites composed of metal atoms in close proximity.

(Figure 2b; Figure S1). In contrast to **CuPd** SSCs, the **Ref-Cu** electrode showed no morphological changes (Figure 2c), indicating that the initial CuPc structure was likely restored after prolonged electrochemical reduction of the CuPc electrode [27]. Energy dispersive X-ray spectroscopy (EDS) in the SEM elemental mapping shows the uniform distribution of Pd, Cu, N, and C on the exposed surface of the electrode, as well as the local high concentration of Pd and Cu in the deposited nanoparticles (Figure S2). The corresponding TEM and HR-TEM images (Figure 2d–f) recorded at different magnifications show the nanostructure of the particles in the formed **CuPd** sample. The related SEM image and the corresponding EDS elemental mapping for CuPc are shown in, Figure S3.

Next, the structure and morphology of the samples were analyzed, and powder X-ray diffraction (pXRD) showed virtually identical diffraction patterns for **CuPd** SSCs samples with different immersion times in $PdCl_2$ solution and reference samples (Figure 2g; Figure S4), and no metal-related peaks were observed. A strong diffraction peak at 26.4°, corresponding to (002) plane of graphite associated with the substrate (carbon paper), and a weak diffraction peak at 54.5° is associated with graphitic carbon [31]. No diffraction peaks corresponding to CuPc (see Figure S5 for reference) were observed in the **CuPd** and the reference samples **Ref-Cu** and **Ref-CuPd**. High-angle annular dark-field and aberration-corrected scanning transmission electron microscopy (HAADF-STEM) combined with EDS was

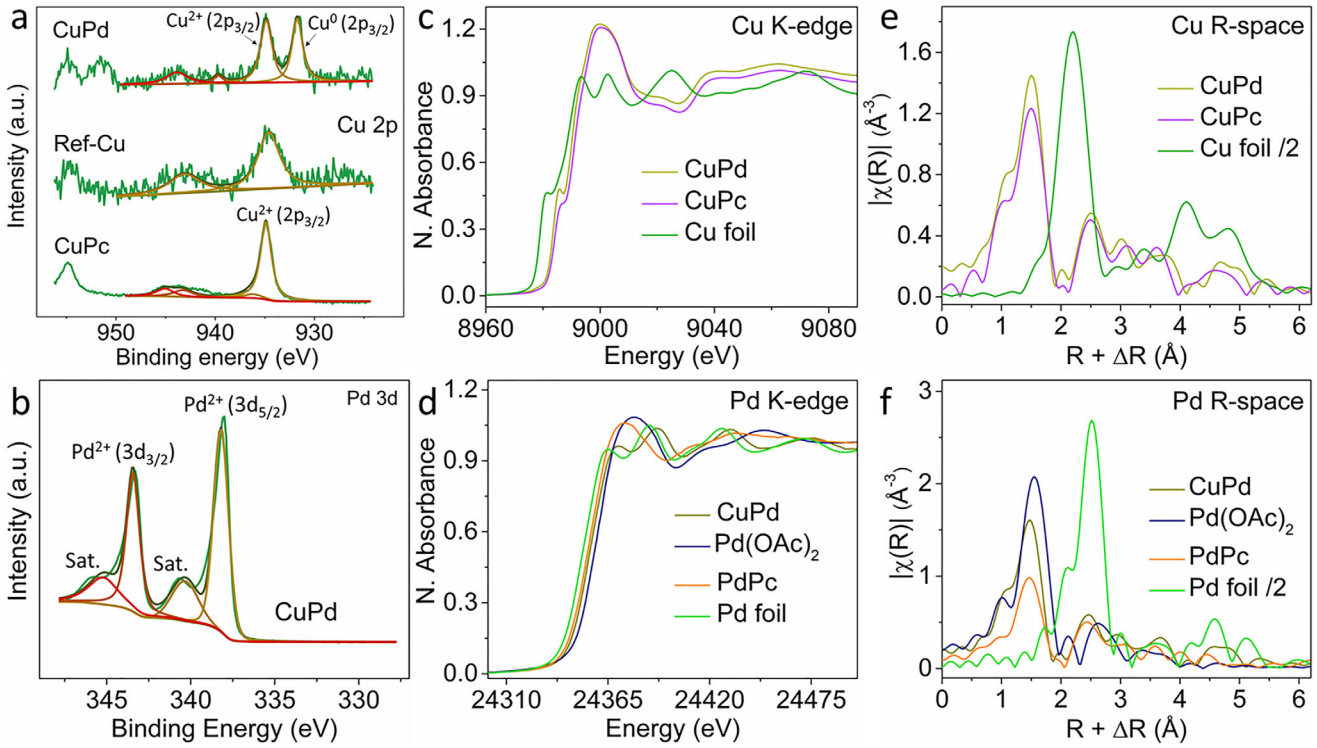

FIGURE 3 | (a) Cu 2p XPS spectra of CuPc, **Ref-Cu**, **CuPd** SSCs. (b) Pd 3d XPS spectra of **CuPd** SSCs. (c) Normalized XANES spectra of the Cu K-edge for the **CuPd** SSCs and reference samples (CuPc and Cu foil). (d) Normalized XANES spectra of the Pd K-edge for **CuPd** SSCs and reference samples (PdPc, $Pd(OAc)_2$, and Pd foil). (e) EXAFS spectra of the Cu K-edge of the **CuPd** SSCs and reference samples (CuPc and Cu foil); (f) EXAFS spectra of the Pd K-edge of the **CuPd** SSCs and reference samples (PdPc, $Pd(OAc)_2$, and Pd foil).

used to obtain further structural information. Figure 2h,i; Figure S6 show representative HAADF-STEM images of **CuPd**. The results showed a high density of bright spots distributed on the darker matrix, corresponding to atomically isolated metal species; large metal clusters/nanoparticles were not detected. The HAADF-STEM image and the corresponding EDS elemental mapping results also show that Cu, Pd, N, and C are uniformly distributed on the macrocyclic structure of the phthalocyanine system (Figure S7). Furthermore, the enlarged HAADF-STEM image (Figure 2i) highlights several regions (marked by yellow circles) containing closely positioned metal atoms, suggesting the presence of numerous proximal dual-atom configurations of neighboring metal atomic sites (while not forming chemically bonded bimetallic sites).

The surface chemical composition and elemental states of the metal species in **CuPd-x** and **CuPc** were investigated by X-ray photoelectron spectroscopy (XPS). The survey spectrum of **CuPd-x** demonstrates the existence of Cu, Pd, N, and C (Figure S8), in line with the EDS elemental mapping results. In the high-resolution Cu-2p spectra of the **CuPd** samples (Figure 3a; Figure S9a), two pairs of XPS peaks at 934.7 and 931.7 eV were deconvoluted in the Cu-$2p_{3/2}$ regions, which are attributed to Cu^{2+} and metallic Cu^0 species originating from the surface reduction of the **CuPc** electrode, respectively. This result indicated the successful reduction of Cu(II) species on the exposed surface of the **CuPc** electrode and revealed the coexistence of Cu^{2+} and metallic Cu^0, where Cu^{2+} was partially reduced during the electrochemical reduction process. In contrast to the **CuPd** samples, only one peak was deconvoluted at 934.9 eV in the Cu-$2p_{3/2}$ regions of the CuPc powder sample, which could be assigned to the Cu^{2+} $2p_{3/2}$ orbital. The Cu-2p spectra of **Ref-Cu** show only one peak at a binding energy of 934.5 eV, which corresponds to the Cu^{2+} $2p_{3/2}$ orbital (Figure 3a). The disappearance of the peak associated with metallic Cu^0 in **Ref-Cu** and the presence of only one peak corresponding to a Cu(II) species revealed the restoration of the original CuPc structure.

In the deconvoluted high-resolution Pd 3d spectra of the **CuPd** samples (Figure 3b; Figure S9b), the fitted peaks at 338.2 and 343.3 eV correspond to the Pd^{2+} $3d_{5/2}$ and Pd^{2+} $3d_{3/2}$ orbitals, respectively, with satellite peaks found at 340.3 and 345.1 eV [32, 33]. In addition, the N 1s XPS spectra of CuPc (Figure S10a) was deconvoluted into two peaks at 398.1 and 400.3 eV assigned to the pyridinic-N and Cu-N, respectively. For **CuPd** samples, an additional peak appeared at 399.7 eV was attributed to pyrrolic-N. Pyrrolic-N, which serves as an anchoring site for metal atoms, could explain the favorable formation of Pd-N moieties. Furthermore, the O 1s region of **CuPd** exhibits two peaks assigned to adsorbed surface hydroxide (OH_{ads}, 532.6 eV) and adsorbed water molecules (H_2O_{ads}, 535.8 eV), as shown in Figure S10b [34]. Based on the above analysis, it is confirmed that the dynamic formation of metallic Cu is reversible in **Ref-Cu** sample and the original structure of CuPc was restored after the prolonged reduction, which agrees well with the previous in situ X-ray absorption spectroscopy (XAS) studies showing that the CuPc structure was restored after the potential of the working electrode was turned off and the electrode was exposed to air [27]. However, in the Cu 2p XPS spectra of the **CuPd** catalysts, the characteristic

peak associated with metallic Cu^0 species was retained, indicating a Cu^0 stabilizing mechanism, possibly by charge-compensation of the Pd cations.

We further investigated the X-ray absorption near-edge structure (XANES) spectra to better understand the electronic structure of the catalysts. Figure 3c shows the Cu K-edge XANES spectra of **CuPd**, together with the reference samples CuPc (containing Cu^{2+}) and a copper foil (containing metallic Cu^0). The Cu absorption edge for **CuPd** is observed at higher energy than for the Cu foil, but lower energy than for CuPc (Figure 3c), implying that the average oxidation state of the Cu species in **CuPd** is between 0 and +2. This is in line with the presence of Cu^{2+} and Cu° clusters, as XAS determines a bulk, average metal oxidation state. Similarly, XANES data of the Pd K-edge of **CuPd** were recorded and compared with Pd foil, PdPc, and $Pd(OAc)_2$, which serve as references for metallic Pd^0 and Pd^{2+}. In **CuPd**, the Pd absorption edge appears at a higher energy than that of metallic Pd foil and closely matches that of PdPc, yet remains lower energy than that of $Pd(OAc)_2$ (Figure 3d), confirming that Pd in **CuPd** is predominantly in the +2 oxidation state. The slightly lower edge position relative to $Pd(OAc)_2$ may arise from differences in the coordinating donor atoms, likely N donors in **CuPd** versus O donors in $Pd(OAc)_2$, which alter the local electronic environment and thus shift the absorption edge [35]. Figure 2e,f show the Fourier transform of the extended X-ray absorption fine structure (FT-EXAFS) spectra of the Cu K-edge and Pd K-edge for **CuPd** sample and reference samples, respectively. The peaks at 2.1 Å for the Cu K-edge and 2.6 Å for the Pd K-edge correspond to Cu-Cu and Pd-Pd interactions of the first shell in the Cu and Pd foils, respectively. These features were not present in **CuPd** and in the reference samples, CuPc PdPc, and $Pd(OAc)_2$. This indicates that the **CuPd** SSCs were dominated by isolated metal atoms, which is consistent with the HAADF-STEM results (Figure 2h,i). Considering that the **CuPd** SSCs have a high number of nitrogen and oxygen functional groups (see XPS data, Figure S10), the peaks at approximately 1.5 Å corresponding to the first shell of the EXAFS spectra can be assigned to M-N/O/C bonding (M = Cu and Pd). The first shell of the Fourier transform of the EXAFS spectrum of **CuPd** SSCs was fitted with Cu-N and Pd-N; Figure S11 and Tables S2 and S3 (SI) summarize the fitting results. A coordination number of approximately 3.9 was obtained for Cu-N, while a value of 3.7 was determined for Pd-N. This observation is in line with our proposed structure, where the Cu or Pd centers are coordinated to a Pc ligand by four nitrogen donor atoms.

2.1 | Electrocatalytic Performance and Product Analysis

The electrocatalytic activities of the **CuPd** SSCs catalysts were evaluated by cyclic voltammetry (CV) in an Ar-saturated 1 M aqueous KOH in the presence or absence 0.5 M glycerol. A three-electrode divided cell setup (membrane: Nafion 117) was used, where the respective catalyst deposited on carbon paper was used as working electrode, Hg/HgO and platinum wire were used as reference and counter electrode, respectively. For comparison, the activities of **Ref-Cu, Ref-CuPd**, and commercial **Pd/C** and **PdPc** were studied under the same conditions. The CV curves during the GOR on **CuPd** SSCs catalyst are characterized by two well-defined anodic peaks in the forward and reverse scans, as shown in Figure 4a. In the forward scan, the anodic peak is attributed to the oxidation of chemisorbed glycerol. In the reverse scan, the anodic peak was primarily associated with the removal of carbonaceous species that were not fully oxidized in the forward scan and the subsequent oxidation of freshly adsorbed glycerol [36]. Also, the peak anodic current density for GOR on **CuPd** SSCs (Figure 4a) was 50 mA/cm^2, which was approximately 15 times higher than that of commercial **Pd/C** (Figure S12), indicating a higher catalytic activity and number of active sites of the **CuPd** SSCs catalyst. The LSV curves (Figure 4b; Figures S12–S18) show that the current densities for GOR on all catalytic electrodes are higher than those for OER, indicating that GOR is thermodynamically (as evidenced by a significant shift in onset potential) and kinetically favored over OER. To achieve a current density of 10 mA cm^{-2} for the OER at the **CuPd** SSCs electrode, an applied potential of 1.66 V is required. For GOR, however, only an applied potential of 1.38 V is required to achieve the same current density, so GOR can be performed at ~0.3 V less positive potentials. This indicates that in the given system, GOR can in principle replace OER and results in lower overall energy consumption.

The **CuPd** SSCs catalyst had a higher GOR activity than the **Ref-Cu** (Figure S13) and **PdPc** (Figure S14) and showed activity comparable to that of the commercial **Pd/C** catalyst (Figure S11). Besides, the **CuPd** SSCs electrode shows a lower onset potential of GOR (1.31 V vs. RHE) than the **Ref-Cu** (1.48 V vs. RHE) and commercial **PdPc** (1.38 V vs. RHE), and a comparable onset potential with **Pd/C** (1.28 V vs. RHE), confirming the facilitating synergistic effect of atomically dispersed Pd ions and dynamically generated Cu clusters in the macrocyclic structure of phthalocyanine. In addition, the CV and LSV curves of **CuPd** SSCs electrodes with different immersion times of reduced CuPc in palladium salt solution show that **CuPd** SSCs and **CuPd-2** catalysts have the highest current density and the lowest onset potential (Figures S14–S17). The CV curves of **Ref-CuPd** (CuPc electrode without electrochemical reduction immersed in a palladium salt solution for 1 h) (Figure S18) showed no detectable anodic peak for the GOR, and the LSV curves exhibited a low current density with an onset potential of 1.39 V vs. RHE, indicating its low electrocatalytic activity and confirming the crucial role of atomically dispersed Pd ions anchored in the in-situ produced macrocyclic structure of phthalocyanine over the possibility of physically adsorbed Pd species in **CuPd** SSCs system.

As shown in Figure S19, the **CuPd** and **CuPd-2** catalysts showed the highest anodic peak current density corresponding to the GOR and a catalytic activity comparable to that of commercial **Pd/C** in the LSV curves (Figure S20) among all electrocatalysts investigated. Moreover, **CuPd** SSCs provided the smallest Tafel slope of 124.1 mV dec^{-1}, which was close to that of **Pd/C** (114.6 mV dec^{-1}) and much lower than that of pure **Ref-Cu** (369.2 mV dec^{-1}), indicating its efficient kinetics for GOR (Figure S21). The highest GOR performance of **CuPd** SSCs was also confirmed by the electrochemical active surface area (ECSA) based on the double-layer capacitance (C_{dl}) measured by CV testing (Figure S22). To exclude the effects of the microstructure and number of active sites, the current density in the LSV curves was normalized by the ECSA (Figure S22). After ECSA normalization, **CuPd** SSCs still exhibited the best GOR

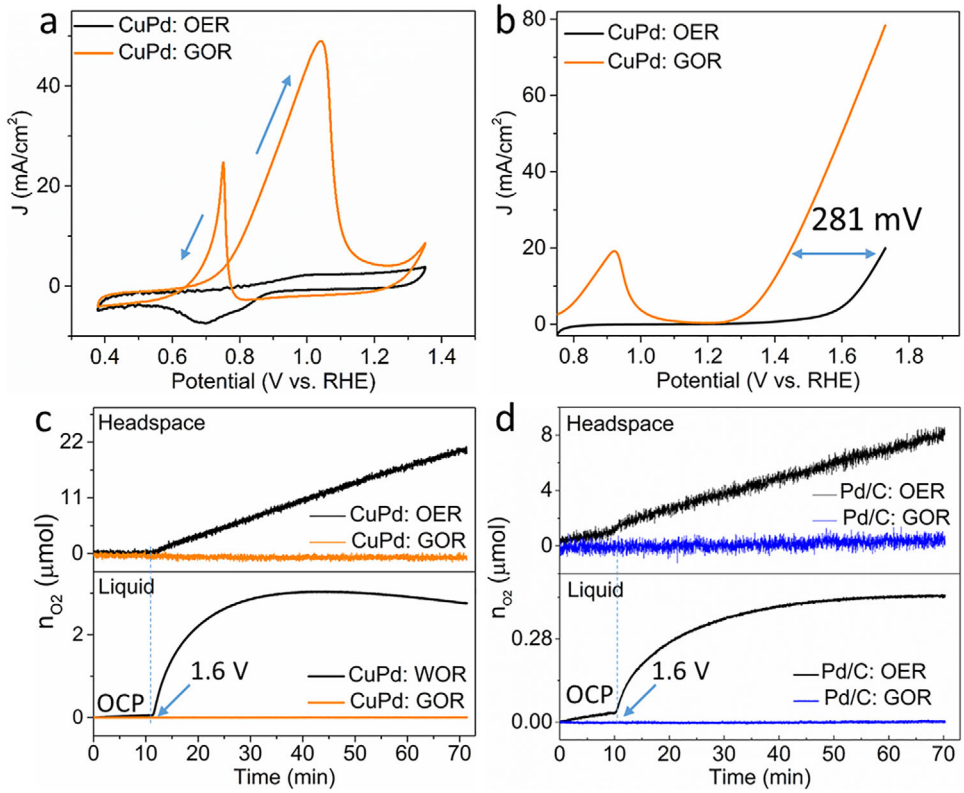

FIGURE 4 | (a) CV (b) LSVs of **CuPd** SSCs during OER and GOR in 1 M aqueous KOH in the presence and absence of 0.5 M glycerol (pH 13.8). Scan rate, 50 mV s^{-1} for CV and 5 mV s^{-1} for LSV. O_2 quantification during OER and GOR for **CuPd** SSCs (c) and commercial **Pd/C** (d).

performance among all samples. These results indicate that **CuPd** SSCs are intrinsically more active for the GOR than **Ref-Cu** and commercial **Pd/C**.

To gain further insight into the competition between OER and GOR, we studied oxygen evolution using an in-situ fluorescent oxygen sensor [37]. OER and GOR electrolysis were performed at 1.6 V vs. RHE for 1 h. For both **CuPd** and **Pd/C**, no oxygen is produced in the presence of glycerol, while in the absence of glycerol, we observe notable OER performance (Figure 4c,d). These data show that oxygen evolution is effectively suppressed by the thermodynamically and kinetically favored GOR.

Next, the GOR products over **CuPd**, **Ref-Cu**, and commercial **Pd/C** and **PdPc** were analyzed using gas chromatography (GC) and nuclear magnetic resonance spectroscopy (^{1}H-, ^{13}C-NMR). The experiments were performed by chronoamperometry (3 h) at potentials between 0.8 to 1.6 V vs. RHE, see Figure S23. Representative ^{1}H- and ^{13}C-NMR spectra of the oxidation products, calibration curves, and GC chromatograms are shown in Figure S24–S30. The ^{1}H NMR spectra showed that the products of the GOR over **CuPd** SSCs electrode mainly contained formate and C3 products (glycolate, glycerate, and lactate) (Figure S24). For formate, we observed maximum FE (82.8%) at a potential of 1.0 V vs. RHE (Figure 5a). Also, C3 products (glycerate, glycolate, lactate) were detected as by-products across the potential range studied. At potentials of 1.4 and 1.6 V, we observed formation of glycolate, most likely formed by a C—C bond cleavage of a C3 precursor.

Product analyses for commercial **Pd/C** (Figure 5b), **Ref-Cu** (Figure 5c) and **PdPc** (Figure S31) also showed that formate was the main product. Comparison of the formate formation for the three catalysts showed significantly higher FEs for **CuPd** compared with the two references (Figure 5d). A similar trend was observed for the FE for C3 product formation (Figure 5e). In addition, **CuPd** showed the highest glycerol conversions at all potentials studied (Figure 5f). **CuPd** compares favorably with most reported nanostructured electrocatalysts for the electrocatalytic GOR-to-C1-C3 product conversion (Table S5). Note that a very low amount of H_2 is detected in the anode compartment under applied potential during glycerol oxidation (Figure 5a–c; Figures S26–S28). Control experiments in the absence of glycerol (Figure S29) also show a minor background H_2 signal under identical anodic polarization conditions. While the exact origin of this hydrogen cannot be unambiguously identified, its magnitude is small and does not affect the catalyst-dependent trends or the conclusions of this study. Plausible origins are diffusion from the cathode side, or processes related to glycerol conversion [38, 39]. Accordingly, hydrogen production is reported in terms of an apparent Faradaic efficiency as a charge-normalized descriptor (Figure 5a–c; Figures S31 and S32), with full experimental details provided in the Supporting Information.

In addition to catalytic activity and product selectivity, long-term stability tests were carried out to investigate the catalytic robustness of **CuPd** SSCs and commercial **Pd/C** catalysts. Under the given conditions, commercial **Pd/C** catalysts show a ~70% drop in current density in a 24 h chronoamperometry test (Figure S33). However, **CuPd** SSCs showed superior stability with a drop

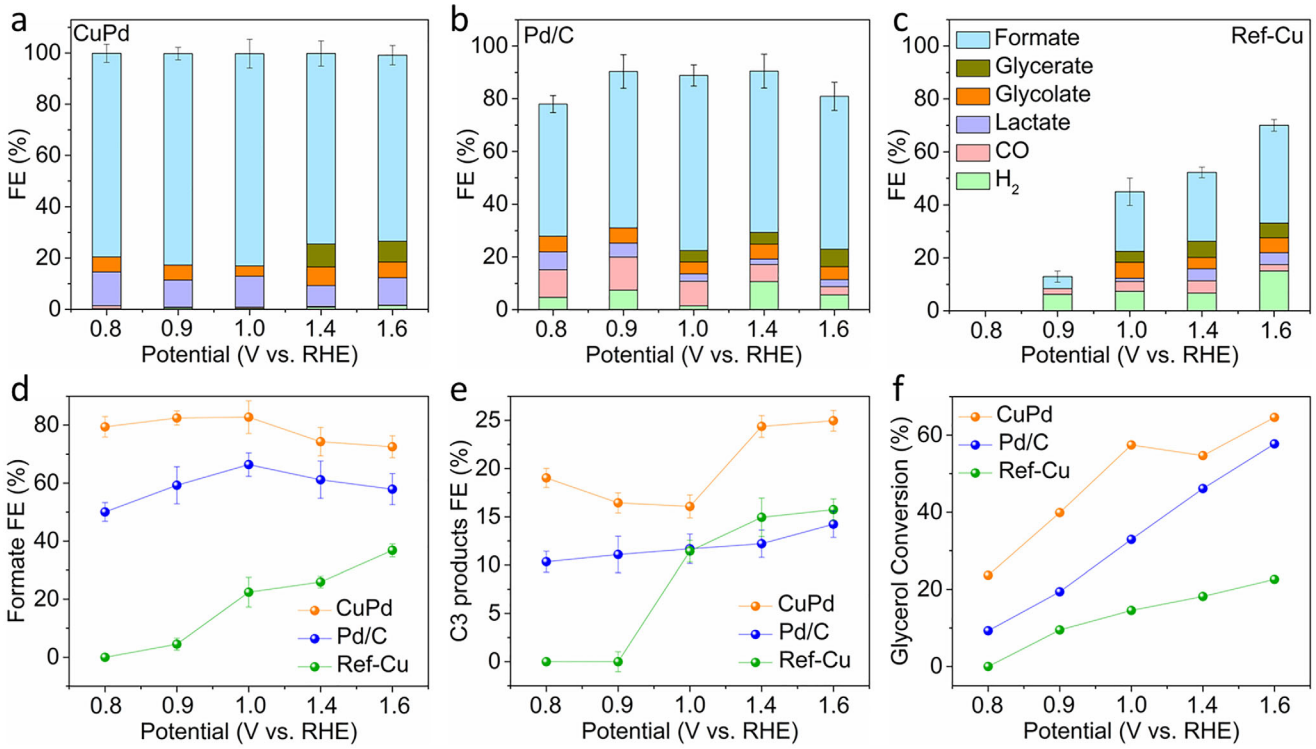

FIGURE 5 | (a) FEs of products from glycerol oxidation at varied potentials for (a) **CuPd** SSCs, (b) commercial **Pd/C**, and (c) **Ref-Cu**. (d and e) FEs for formate and C3 products on **CuPd** SSCs, **Ref-Cu**, and commercial **Pd/C** at varied potentials; (f) Glycerol conversion at different potentials for **CuPd** SSCs, **Ref-Cu**, and commercial **Pd/C** in 1 M aqueous KOH with 0.5 M glycerol (pH 13.8) during a chronoamperometric measurement over 3 h.

of only 24% during a 144 h chronoamperometry (1.6 V vs. RHE), confirming the robustness of the **CuPd** SSCs anode (Figure 6a). The drop in current density could be due to the consumption of glycerol and OH^-, as confirmed by the decreased pH (13.6) of the electrolyte. In this study, formate was obtained as the main product throughout the durability measurement, while the FE for formate decreased from 73% to 60% over the course of the electrolysis (Figure 6b). We assign this to the changes of reaction conditions (substrate concentration, intermediate formation, electrolyte pH). The FEs for the C3 products increased from 25% to 36% during the experiment, likely due to the dynamic structural changes of the catalyst under the reaction conditions. During the 144 h GOR electrolysis, we note nearly linear increases for all products studies, providing further evidence for the robust GOR performance of the **CuPd** electrode (Figure 6c,d; Figure S34). To further assess catalyst stability beyond current density metrics, potentiostatic electrolysis was performed using both an aged catalyst in fresh electrolyte (Figure S35) and a fresh catalyst in aged electrolyte, Figure S36). Reproducible chronoamperometric responses, unchanged ^{1}H-NMR product spectra, and stable Faradaic efficiencies across multiple 24 h cycles confirm that catalytic activity and product selectivity are maintained, while minor variations during electrolyte reuse are due to partial glycerol consumption. These results indicate that long-term performance is governed primarily by changes in reaction conditions rather than catalyst degradation. Consistent with these findings, cyclic stability tests over 2000 CV cycles also showed that the anodic peak current for GOR remained largely stable for the first 500 cycles and declined gradually due to glycerol consumption rather than intrinsic catalyst degradation (Figure S37). Upon refreshing the electrolyte, CV and LSV measurements demonstrated full recovery of catalytic activity, corroborated by ^{1}H-NMR analysis confirming substrate consumption as the main factor (Figure S37).

To further elucidate the mechanistic basis for the observed activity and stability of the **CuPd** catalyst, we performed density functional theory (DFT) calculations, projected density of states (PDOS), and Bader charge analyses on **Ref-Cu**, **PdPc**, and **CuPd** dual-site models (Figures S38 and S39 and Table S4). Optimized geometries indicate that Pd sites preferentially adsorb OH species, whereas Cu sites stabilize C-C-containing intermediates, and the calculated free-energy diagrams show that the **CuPd** dual-site model exhibits the lowest overall reaction barriers for glycerol oxidation (Figure 7a). PDOS analysis reveals strong hybridization and overlap of Cu and Pd d-states near the Fermi level, reflecting electronic coupling between the metals (Figure S39). Compared with **Ref-Cu**, Pd incorporation shifts the Cu d-band center and redistributes electronic states, consistent with charge transfer and orbital interactions at the Cu-Pd interface. Bader charge analysis and nearly spin-symmetric Cu PDOS further indicate delocalized charge and suppression of local magnetic moments. Collectively, these results demonstrate that Pd not only tunes surface energetics to stabilize intermediates and suppress deep C-C bond cleavage, but also electronically compensates and stabilizes Cu^0 species. These combined theoretical insights strongly support the proposed dual-site and charge-compensation mechanisms and are fully consistent with our experimental selectivity and stability trends.

Operando XAS was used to probe the oxidation state and local structure of Cu sites during the GOR. The Cu K-edge XANES

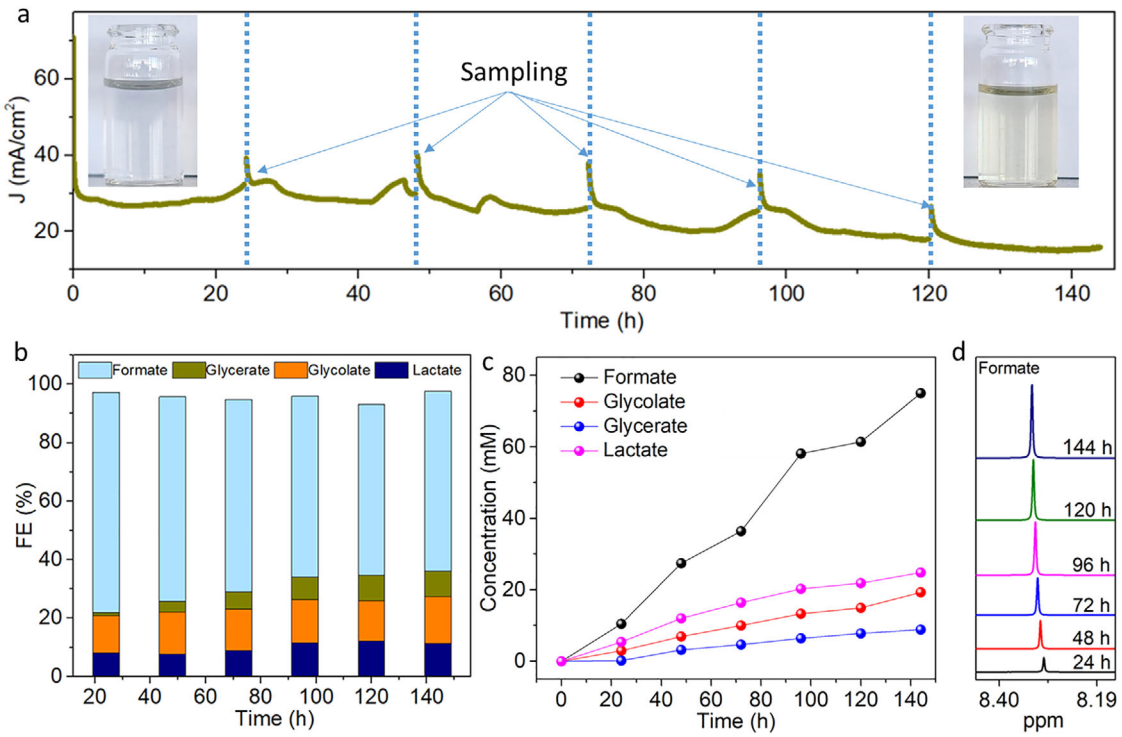

FIGURE 6 | (a) Long-term GOR stability test for **CuPd** at an applied potential of 1.6 V vs. RHE. The inset pictures show the electrolyte before and after 144 h electrolysis. (b) FEs for formate, glycolate, glycerate and lactate obtained from the long-term stability electrolysis shown in (a). (c) Product concentrations for formate, glycolate, glycerate and lactate obtained from the long-term stability electrolysis shown in (a). (d) ^{1}H-NMR spectra of formate taken during the GOR electrolysis shown in (a).

spectra (Figure 7b) show negligible changes in edge position and white-line intensity between 0.8–1.6 V, indicating a largely stable Cu oxidation state under reaction conditions. The corresponding EXAFS spectra (Figure 7c) lack the Cu-Cu metallic peak (~2.2 Å) of Cu foil, confirming single-site nature of Cu sites. The main peak at ~1.5 Å, assigned to Cu-N/O/C coordination, remains unchanged with potential, indicating structural stability. These results reveal that Cu acts as an electronically adaptive yet structurally robust reservoir and stabilizing active sites during GOR.

Operando studies with attenuated total reflectance Fourier transform infrared spectroscopy (ATR-FTIR) were used to further monitor the intermediate species formed during GOR at the **CuPd** electrode at different potentials. As shown in Figure 7d, the activation of the hydroxyl functional group of glycerol at the catalytically active site with increased applied potentials was confirmed by the appearance of a peak at 1085 cm^{-1}, which represents the C-O stretching of the alcohols [40]. This signal was not observed at the open circuit potential (OCP). The direct oxidation of glycerol to glyceraldehyde was indicated by a characteristic vibrational peak at 1149 cm^{-1}, which corresponds to glyceraldehyde (GLA) [41]. This indicates that the GLA intermediate was further oxidized to form C1-C3 products. As the potential was increased (above 0.8 V vs. RHE), a signal at 1214 cm^{-1} emerged, revealing the formation of a carboxylate moiety [41]. This is indicative for the formation of carboxylate species (e.g., glycolate, glycerate, lactate and formate), and is further supported by a signal at 1581 cm^{-1} (Figure 7e) corresponding to the asymmetric carboxylate C-O stretching [40]. The peaks at 1330 cm^{-1} and 1353 cm^{-1} were assigned to the symmetric C—O stretching and COO rocking of oxidized glycerol intermediates. In addition, the peak at 1417 cm^{-1} corresponds to the asymmetric O-C-O stretching band is associated with the C3 products [42]. Notably, a peak around 1600 cm^{-1} was observed, assigned to intermolecular hydrogen bonds. This peak increased with potential, indicating that the surface OH^- concentration also increased because of the negative charge favoring alkoxide adsorption on the metal surface. The presence of carboxylate intermediates is further evidenced by peaks around 2100 cm^{-1} (Figure S40), which correspond to CO species, confirming the production of CO as a minor product [43]. Of additional note, the intensity of the vibrational peak at 2100 cm^{-1}, corresponding to CO formation, increased with increasing potential from 1.2–1.7 V vs. RHE, indicating that some of the intermediate species were fully oxidized at potentials above 1.2 V. This observation was also consistent with the ^{13}C-NMR results (Figure S25), where a smaller peak related to CO_3^{2-} was detected. Finally, the increased OH^- concentration at the electrode surface was further confirmed by the appearance of a peak around 3200 cm^{-1}, assigned to the OH^- band [44], which was higher at increased potentials (Figure 7f). Based on the above experimental results, the possible processes of GOR in alkaline media follow the path shown in Figure 7g [8, 18].

To complement the operando ATR-FTIR analysis of the **CuPd** electrode, in-situ FTIR spectra were recorded for **Ref-Cu** and **PdPc** to clarify their roles during glycerol oxidation (Figure S41). For **Ref-Cu**, a band at ~1072 cm^{-1} corresponds to the C-O stretching of alcohols, confirming hydroxyl activation (Figure S41a). At

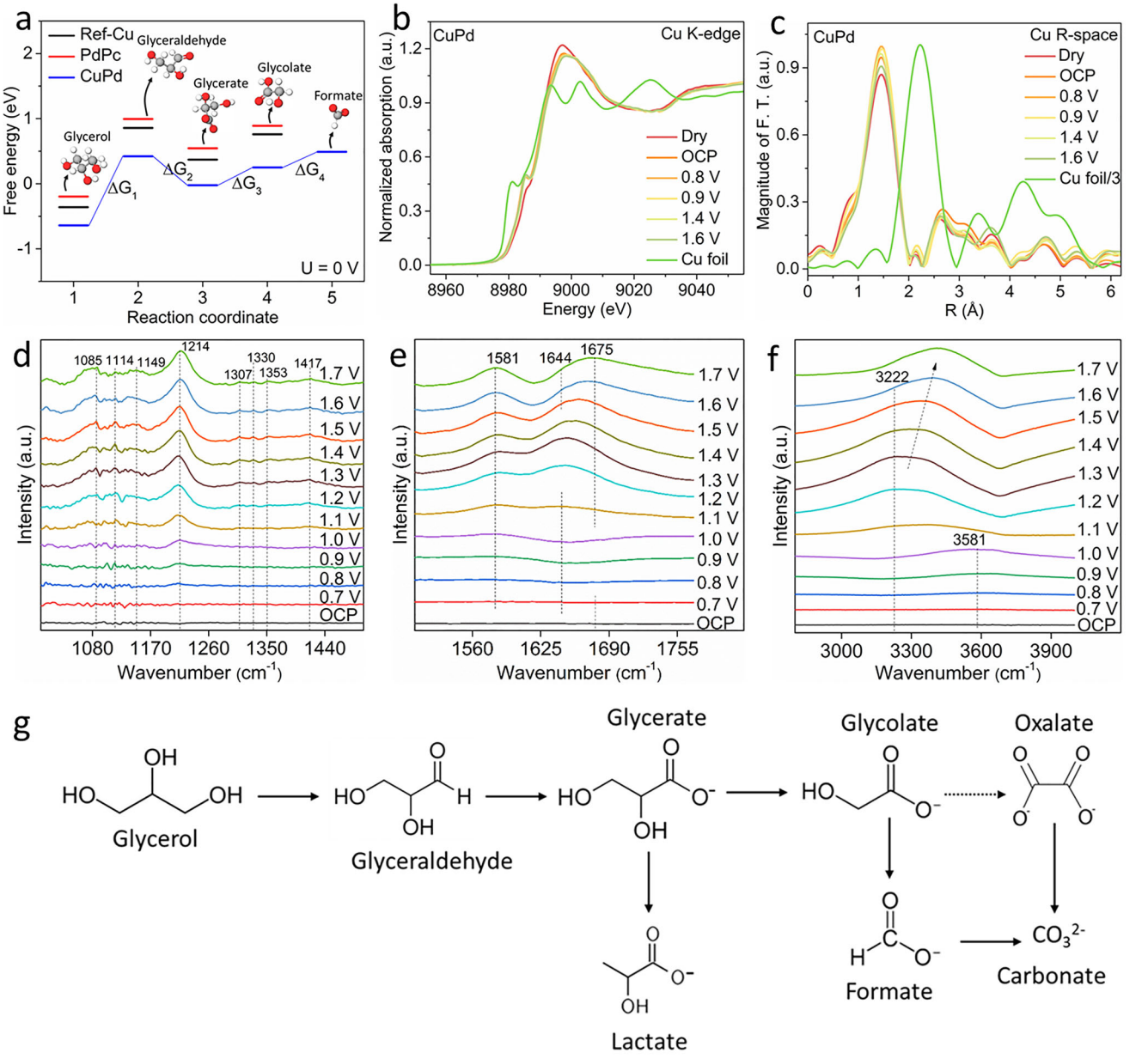

FIGURE 7 | (a) DFT-calculated free energy profiles (U = 0 V) for glycerol oxidation on **Ref-Cu**, **PdPc**, and **CuPd** SSCs. (b) Operando XANES spectra of Cu K-edge and (c) the corresponding EXAFS spectra of **CuPd** SSCs under GOR conditions in 1.0 M KOH containing 0.5 M glycerol. (d-f) In situ ATR-FTIR spectra at different potentials. (g) Proposed glycerol oxidation pathway to C1-C3 products over **CuPd** SSCs highlighting dual-site Cu-Pd synergy.

higher potentials (≥1.2 V vs. RHE), additional features at 1222 and 1365 cm^{-1} appear, assigned to carboxylate formation and symmetric COO^- rocking of oxidized intermediates. A peak at 1639 cm^{-1}, attributed to glyceraldehyde, shifts blue with increasing potential, indicating progressive oxidation (Figure S41b). The absence of the OH^- stretching band for **Ref-Cu** (Figure S41c) aligns with its lower activity and weaker hydroxide adsorption. In contrast, **PdPc** exhibits stronger and more defined vibrations at 1037 cm^{-1} (C-O stretching), 1108 cm^{-1} (glyceraldehyde formation), and 1450 cm^{-1} (symmetric COO^- rocking), along with a broad OH^- stretching band at ~3200 cm^{-1} that intensifies at higher potentials (Figure S41d–f). These observations confirm enhanced OH^- adsorption and more efficient oxidation of glycerol intermediates on **PdPc** relative to **Ref-Cu**, reinforcing the operando ATR-FTIR findings for **CuPd** and supporting the proposed synergistic mechanism.

2.2 | Post-Catalytic Analysis

The structural and electronic stability of the **CuPd** SSC catalyst under prolonged GOR conditions was evaluated through chronoamperometric and cyclic stability tests, followed by detailed post-reaction characterizations using SEM, EDS, XRD, XPS, and ICP-OES (Figures S42–S47 and Table S5). Post-stability analysis was also performed to investigate whether the reactive metal species (Pd and Cu) retained or lost their activity during the long-term electrocatalysis. The SEM image (Figure S42) revealed

no noticeable change in morphology, and the corresponding EDS elemental mapping indicated a homogeneous distribution of the elements Pd, Cu, N and C in **CuPd** electrode. The XRD pattern (Figure S43) showed similar diffraction peaks to the original **CuPd**, with no diffraction peaks related to clusters or oxides. The XPS and ICP-OES analyses of **CuPd** after a 144 h stability test (Figures S44–S46 and Table S5) confirmed the presence of Cu and Pd with the respective dominant oxidation state +2. Our results show that the original morphology, crystal structure, elemental composition, and oxidation states (with the exception of Cu 2p, where the restructuring of CuPc was observed as the Cu(II) species dominated and a minor peak associated with metallic Cu(0) was observed, as revealed by XPS) were maintained, and the **CuPd** SSCs catalyst after the stability test had similar properties as before the catalysis application. The reversible oxidation state of the Cu(II) species and the disappearance of the peak associated with metallic Cu^0 in the original sample could be due to the positive potential used for the stability test during the GOR, which can also oxidize the reduced Cu species. Post-cyclic stability characterization using XPS also verified the preservation of the surface chemical composition and dominant Cu^{2+}/Pd^{2+} states (Figure S47). These results demonstrate that the **CuPd** SSC catalyst retains its dual-atom configuration, electronic structure, and high catalytic performance under extended GOR conditions. The experimental observations align with theoretical insights into the dual-site synergistic and charge-compensation mechanisms, highlighting the robustness and electrocatalytic resilience of the **CuPd** SSC system for long-term operation.

3 | Discussion

We synthesized **CuPd** SSCs catalysts with a high density of atomically distributed Pd-N_4/Cu-N_4 sites by simple electrochemical reduction of a CuPc precursor without the agglomeration of reactive metal species as shown by the EXAFS analysis (Figure 3e,f) and the HAADF-STEM results of **CuPd** SSCs (Figure 2h,I; Figure S6). These atomically dispersed dual-metal sites catalyze the GOR with remarkably high activity, selectivity, and stability compared to commercial **Pd/C**, **PdPc** and **Ref-Cu** samples. The high catalytic activity and selectivity of **CuPd** SSCs originates from both the greater number of active sites, as indicated by a higher ECSA value (see Figure S22d), and enhanced intrinsic activity, as evidenced by the higher current density and lower onset potential after normalizing the LSV curves with ECSA (Figure S22f). The in situ fluorescent oxygen sensor studies during the OER and GOR revealed that GOR completely suppresses/blocks OER. It is also noteworthy that the GOR is thermodynamically and kinetically favored over the OER and can be performed at ~0.3 V less positive potential than the OER, as evidenced by the LSV curves in Figure 4b. In combination with the experimental results presented above and previous reports (Table S6), the reaction pathway for the GOR on **CuPd** SSCs catalyst was proposed, as shown in Figure 7g. Glycerol is first oxidized to glyceraldehyde, which in turn is oxidized to a C3 product such as glycerate [45, 46]. Glycerate is then oxidized to lactate or undergoes a C-C bond break to form glycolate and the main product formate. Glycerate and lactate can be generated from one terminal C-bonded intermediate on the **CuPd** SSCs, and the subsequent further oxidation may lead to the formation of the C1 product, such as formate. The formate product can also be formed by the oxidation of two terminal carbon-bonded intermediates, cleaving the C-C bond, which is usually found on nanostructured commercial **Pd/C** catalysts. As a result, these intermediates and their further oxidized CO products can lead to a rapid loss of activity, as observed for **Pd/C** catalysts. This result highlights the advantage of an atomically dispersed single-site catalyst for the partial oxidation of glycerol to a range of C1-C3 products. Another important aspect of the **CuPd** SSCs is that the introduction of atomically dispersed Pd single sites promotes the adsorption of OH species of the hybrid catalyst, which not only facilitates the dehydrogenation of glycerol, leading to improved GOR activity, but also promotes the production of C1-C3 products at relatively low potentials, thereby avoiding the further oxidation of C1-C3 products. In addition, the number of two terminal carbon atoms of the intermediates on the **Pd/C** electrode enabled by neighboring Pd-Pd reactive sites is largely reduced in the **CuPd** SSCs electrode because of the atomically distributed single sites of Pd and Cu, resulting in improved C1-C3 selectivity of the **CuPd** SSCs for GOR over a wide range of applied potentials. These results demonstrate that the atomic-scale single sites of Pd and Cu not only effectively increase the adsorption capacity of OH species but also optimize the glycerol adsorption configuration, which largely avoids C-C bond cleavage and the formation of poisonous carbonaceous intermediates, thereby enhancing the activity and C1-C3 selectivity for GOR. DFT calculations provide mechanistic insights into the observed catalytic behavior. Pd sites preferentially bind OH^-, while Cu stabilizes C-C-containing intermediates. Reaction barriers for glycerol oxidation are lower on the **CuPd** dual sites than on single metals (**Ref-Cu** and **PdPc**), and PDOS/Bader charge analyses show synergistic electronic interactions that enhance selectivity and stability, consistent with the experimentally observed high selectivity and stability. This theoretical insight aligns with the *operando* FTIR observations: the pronounced OH^- band in Pd-containing systems (Figure 7f; Figure S41f) and its absence in **Ref-Cu** (Figure S41c) confirm that hydroxyl adsorption predominantly occurs on Pd sites, with Cu facilitating the process through electronic coupling. *Operando* XAS and FTIR further provided experimental validation. Cu K-edge XAS confirms that Cu retains its atomically dispersed structure under working potentials, while ATR-FTIR detects glycerol oxidation intermediates and adsorbed OH^-. Key IR bands indicate formation of glyceraldehyde, glycerate, lactate, glycolate, and formate, with minimal CO-type signals at high potentials. These results confirm that **CuPd** SSCs promote sequential dehydrogenation and controlled C-C cleavage, enabling selective C1-C3 product formation. It is also worth mentioning that most of the literature reports published so far for GOR are based on nanostructured noble metals (Table S6) [8, 16, 36, 42, 44, 46–58]. In particular, this work represents the first use of atomically dispersed bimetallic single-site catalysts for the partial oxidation of glycerol to replace anodic OER-based hydrogen production in water electrolysis technology. We expect this type of catalyst to be exploited as an alternative to nanostructure-based catalysts, in which the activity and selectivity are intrinsically limited by C—C bond cleavage (deep oxidation) and the formation of poisonous carbonaceous intermediates in the scaling relationship between GOR and OER. Taken together, the experimental and theoretical results demonstrate that the atomic-level Cu-Pd dual-site architecture synergistically optimizes surface energetics and electronic structure to enhance OH adsorption, stabilize reaction intermediates, and prevent deep C—C bond cleavage.

The cooperative interaction between Cu and Pd atoms promotes both selectivity and durability, highlighting the robustness and electrochemical resilience of the **CuPd** SSCs system for long-term glycerol oxidation. Based on the above results, replacing anodic OER with GOR-based hydrogen production in water electrolysis technology using such atomically engineered catalysts can save an enormous amount of energy required for water electrolysis while producing value-added chemical products.

4 | Conclusion

We report a bottom up molecular route for the scalable synthesis of bimetallic **CuPd** single-site catalysts by electrochemical reduction of a molecular CuPc species. Modification of this species with Pd^{2+} results in formation of a bimetallic CuPd electrocatayst with remarkable glycerol oxidation reaction performance. The electrocatalytic activity of **CuPd** can be attributed to the unique, well-defined arrangement of the reactive metal sites. The synergetic properties of the Cu single site act as a structural site and the Pd single site serves as a catalytic site in **CuPd** system, which could increase the amount of OH_{ads} groups of the terminal carbon of the glycerol on the catalyst surface, leading to preferential production of C1-C3 products. Thus, the **CuPd** SSCs has demonstrated very promising catalytic activity for GOR, with a preference toward formate (FE: 82.8%) and C3 (FE: 16.5%) at 1 V vs. RHE in an alkaline electrolyte. The **CuPd** catalyst reached high anodic current densities (50 mA cm^{-2}) and showed stable product formation over 144 h electrocatalytic operation. Mechanistic studies combining DFT and *operando* spectroscopy reveal that dual Cu-Pd sites lower glycerol oxidation barriers, promote synergistic electronic interactions, and maintain atomic dispersion under reaction conditions, enabling sequential dehydrogenation with controlled C-C bond cleavage and minimal CO-type intermediates. Our findings suggest a promising approach to synthesize bimetallic single-site catalysts with high metal loadings for different catalytic applications.

Author Contributions

S.A.C. E.O.O and C.S. conceptualized the study. S.A.C. and E.O.O performed syntheses and characterization. S.A.C., E.O.O., T.R.S. K.P., P.H., and K.S. performed general characterization and electrochemical analyses. M.L. carried out oxygen quantification studies. K.L. conducted the in-situ ATR-FTIR measurement. S.A.C. and S.T.C. performed GC analysis. S.A.C. and T.R.S. performed NMR analysis. S.R. performed elemental analyses. J.B. performed XPS analysis. E.E., S.S.A., K.C., and R.L. performed electron microscopic analysis and data interpretation. M.C.T carried out the computational calculations. K.L., C.C.C. and C.Y.C. performed XAS analyses and data fitting. B.J.H. supported synchrotron-based XAS and in-situ ATR-FTIR studies and the validation of the data. C.S. acquired funding and supervised the project. All authors cowrote the manuscript.

Acknowledgements

Financial support by the Deutsche Forschungsgemeinschaft DFG (390874152 (J.B., U.K., C.S.), 501934135, 565959534, 565959534 (C.S.), and 569714822 (S.S.A), the German Federal Ministry for Education and Research (BMBF) through the Clusters4Future Initiative (cluster ETOS, project ELFION, project no 03ZU1205EA (C.S.)), the Carl Zeiss Stiftung (project "Halocycles", project no P2021-10-007 (C.S.)), and the National Science and Technology Council (NSTC) (Project "Resail", Project no 114-2639-E-011-001-ASP (BJH) and 114-2628-E-024-001-MY3 (MCT)) is gratefully acknowledged. S.A.C., E.O.O., R.L., S.R. and S.S.A gratefully acknowledge the Alexander von Humboldt Foundation for postdoctoral fellowships (1214642, 1212758, 1231513, 1186323, and 1229071). The authors gratefully acknowledge Leon Prädel for assistance with XPS. The National Synchrotron Radiation Research Centre (NSRRC) is gratefully acknowledged for providing synchrotron radiation beamtime at the beamline TPS-44A (Quick EXAFS). Computational resources were provided by the National Center for High-Performance Computing (NCHC). C.S gratefully acknowledges the Gutenberg Research College Mainz and the Top-Level Research Area SusInnoScience for financial support.

Conflicts of Interest

The authors declare no conflict of interest.

Data Availability Statement

The data that support the findings of this study are openly available in zenodo.org at https://doi.org/10.5281/zenodo.16637521, reference number 16637521.

References

1. M. Chatenet, B. G. Pollet, D. R. Dekel, et al., "Water electrolysis: From textbook knowledge to the latest scientific strategies and industrial developments," *Chemical Society Reviews* 51 (2022): 4583–4762, https://doi.org/10.1039/D0CS01079K.

2. A. J. Shih, M. C. Monteiro, F. Dattila, et al., "Water electrolysis," *Nature Reviews Methods Primers* 2 (2022): 84, https://doi.org/10.1038/s43586-022-00164-0.

3. H.-F. Wang, L. Chen, H. Pang, S. Kaskel, and Q. Xu, "MOF-derived electrocatalysts for oxygen reduction, oxygen evolution and hydrogen evolution reactions," *Chemical Society Reviews* 49 (2020): 1414–1448, https://doi.org/10.1039/C9CS00906J.

4. Z. P. Wu, X. F. Lu, S. Q. Zang, and X. W. Lou, "Non-Noble-Metal-Based Electrocatalysts Toward the Oxygen Evolution Reaction," *Advanced Functional Materials* 30 (2020): 1910274, https://doi.org/10.1002/adfm.201910274.

5. L. Fan, B. Liu, X. Liu, N. Senthilkumar, G. Wang, and Z. Wen, "Recent Progress in Electrocatalytic Glycerol Oxidation," *Energy Technology* 9 (2021): 2000804, https://doi.org/10.1002/ente.202000804.

6. G. Dodekatos, S. Schünemann, and H. Tüysüz, "Recent Advances in Thermo-, Photo-, and Electrocatalytic Glycerol Oxidation," *ACS Catalysis* 8 (2018): 6301–6333, https://doi.org/10.1021/acscatal.8b01317.

7. M. Simões, S. Baranton, and C. Coutanceau, "Electrochemical Valorisation of Glycerol," *Chemsuschem* 5 (2012): 2106–2124.

8. L. Fan, Y. Ji, G. Wang, et al., "High Entropy Alloy Electrocatalytic Electrode Toward Alkaline Glycerol Valorization Coupling With Acidic Hydrogen Production," *Journal of the American Chemical Society* 144 (2022): 7224–7235, https://doi.org/10.1021/jacs.1c13740.

9. M. R. Monteiro, C. L. Kugelmeier, R. S. Pinheiro, M. O. Batalha, and A. da Silva César, "Glycerol From biodiesel production: Technological paths for sustainability," *Renewable and Sustainable Energy Reviews* 88 (2018): 109–122, https://doi.org/10.1016/j.rser.2018.02.019.

10. Y. Zhou, Y. Shen, J. Xi, and X. Luo, "Selective Electro-Oxidation of Glycerol to Dihydroxyacetone by PtAg Skeletons," *ACS Applied Materials & Interfaces* 11 (2019): 28953–28959, https://doi.org/10.1021/acsami.9b09431.

11. D. Wang, Q. Li, C. Han, Z. Xing, and X. Yang, "Single-atom ruthenium based catalyst for enhanced hydrogen evolution," *Applied Catalysis B: Environmental* 249 (2019): 91–97, https://doi.org/10.1016/j.apcatb.2019.02.059.

12. R. Liu and C. Streb, "Polyoxometalate-Single Atom Catalysts (POM-SACs) in Energy Research and Catalysis," *Advanced Energy Materials* 11 (2021): 2101120, https://doi.org/10.1002/aenm.202101120.

13. C. Cai, S. Han, Q. Wang, and M. Gu, "Direct Observation of Yolk–Shell Transforming to Gold Single Atoms and Clusters With Superior Oxygen Evolution Reaction Efficiency," *ACS Nano* 13 (2019): 8865–8871.

14. S. Ren, X. Cao, Z. Jiang, et al., "Single-Atom Catalysts for Electrochemical Applications," *Chemical Communications* 59 (2023): 2560–2570, https://doi.org/10.1039/D3CC00005B.

15. Z. Song, L. Zhang, K. Doyle-Davis, X. Fu, J. L. Luo, and X. Sun, "Recent Advances in MOF-Derived Single Atom Catalysts for Electrochemical Applications," *Advanced Energy Materials* 10 (2020): 2001561, https://doi.org/10.1002/aenm.202001561.

16. Y. Wang, Y.-Q. Zhu, Z. Xie, et al., "Efficient Electrocatalytic Oxidation of Glycerol via Promoted OH* Generation Over Single-Atom-Bismuth-Doped Spinel Co 3 O 4," *ACS Catalysis* 12 (2022): 12432–12443, https://doi.org/10.1021/acscatal.2c03162.

17. J. Zhu, X. Li, X. Yang, et al., "Facile Preparation of Nitrogen-Doped Carbon Spheres With Wrinkled Cage-Supported Single-Atom Copper Catalysts for Selective Oxidation of Glycerol to Formic Acid," *ACS Sustainable Chemistry & Engineering* 10 (2022): 17177–17186, https://doi.org/10.1021/acssuschemeng.2c05002.

18. H. Yu, W. Wang, Q. Mao, et al., "Pt single atom captured by oxygen vacancy-rich NiCo layered double hydroxides for coupling hydrogen evolution With selective oxidation of glycerol to formate," *Applied Catalysis B: Environmental* 330 (2023): 122617, https://doi.org/10.1016/j.apcatb.2023.122617.

19. S. Zhu, X. Hu, L. Zhang, and M. Shao, "Impacts of Perchloric Acid, Nafion, and Alkali Metal Ions on Oxygen Reduction Reaction Kinetics in Acidic and Alkaline Solutions," *The Journal of Physical Chemistry C* 120 (2016): 27452–27461, https://doi.org/10.1021/acs.jpcc.6b09769.

20. L. Zhang, Q. Chang, H. Chen, and M. Shao, "Recent advances in palladium-based electrocatalysts for fuel cell reactions and hydrogen evolution reaction," *Nano Energy* 29 (2016): 198–219, https://doi.org/10.1016/j.nanoen.2016.02.044.

21. X. Liang, N. Fu, S. Yao, Z. Li, and Y. Li, "The Progress and Outlook of Metal Single-Atom-Site Catalysis," *Journal of the American Chemical Society* 144 (2022): 18155–18174, https://doi.org/10.1021/jacs.1c12642.

22. F. Luo, A. Roy, M. T. Sougrati, et al., "Structural and Reactivity Effects of Secondary Metal Doping Into Iron-Nitrogen-Carbon Catalysts for Oxygen Electroreduction," *Journal of the American Chemical Society* 145 (2023): 14737–14747, https://doi.org/10.1021/jacs.3c03033.

23. Q. Zhang, X. Zhang, B. Liu, et al., "Active Hydroxyl-Mediated Preferential Cleavage of Carbon-Carbon Bonds in Electrocatalytic Glycerol Oxidation," *Angewandte Chemie* 137 (2025): 202420942, https://doi.org/10.1002/ange.202420942.

24. Y. Guo, M. Wang, Q. Zhu, D. Xiao, and D. Ma, "Ensemble effect for single-atom, small cluster and nanoparticle catalysts," *Nature Catalysis* 5 (2022): 766–776, https://doi.org/10.1038/s41929-022-00839-7.

25. W. Ren, X. Tan, C. Jia, et al., "Electronic Regulation of Nickel Single Atoms by Confined Nickel Nanoparticles for Energy-Efficient CO 2 Electroreduction," *Angewandte Chemie* 134 (2022): 202203335, https://doi.org/10.1002/ange.202203335.

26. L. Huang, Y. Q. Su, R. Qi, et al., "Boosting Oxygen Reduction via Integrated Construction and Synergistic Catalysis of Porous Platinum Alloy and Defective Graphitic Carbon," *Angewandte Chemie* 133 (2021): 25734–25741, https://doi.org/10.1002/ange.202111426.

27. Z. Weng, Y. Wu, M. Wang, et al., "Active sites of copper-complex catalytic materials for electrochemical carbon dioxide reduction," *Nature Communications* 9 (2018): 415, https://doi.org/10.1038/s41467-018-02819-7.

28. S. A. Chala, R. Liu, E. O. Oseghe, et al., "Selective Electroreduction of CO 2 to Ethanol via Cobalt–Copper Tandem Catalysts," *ACS Catalysis* 14 (2024): 15553–15564, https://doi.org/10.1021/acscatal.4c05286.

29. S. A. Chala, K. Lakshmanan, W.-H. Huang, et al., "Cooperative dual single atom Ni/Cu catalyst for highly selective CO2-to-ethanol reduction," *Applied Catalysis B: Environment and Energy* 358 (2024): 124420, https://doi.org/10.1016/j.apcatb.2024.124420.

30. K. Lakshmanan, W. H. Huang, S. A. Chala, et al., "Generating Multi-Carbon Products by Electrochemical CO 2 Reduction via Catalytically Harmonious Ni/Cu Dual Active Sites," *Small* 20 (2024): 2307180, https://doi.org/10.1002/smll.202307180.

31. D. Ye, Q. Lan, Q. Liao, et al., "Role of defects and oxygen-functional groups in carbon paper cathode for high-performance direct liquid fuel cells," *Carbon* 192 (2022): 170–178, https://doi.org/10.1016/j.carbon.2022.02.053.

32. O. Lupan, V. Postica, M. Hoppe, et al., "PdO/PdO 2 functionalized ZnO : Pd films for lower operating temperature H 2 gas sensing," *Nanoscale* 10 (2018): 14107–14127, https://doi.org/10.1039/C8NR03260B.

33. T. J. Wang, F. M. Li, H. Huang, et al., "Porous Pd-PdO Nanotubes for Methanol Electrooxidation," *Advanced Functional Materials* 30 (2020): 2000534, https://doi.org/10.1002/adfm.202000534.

34. B. Jeong, D. Lee, J.-I. Park, and S. M. Lee, "Near ambient pressure XPS investigation of hydrous palladium oxide Under water and oxygen gas environments," *Journal of Physics D: Applied Physics* 54 (2021): 324001, https://doi.org/10.1088/1361-6463/ac0183.

35. B. L. Geoghegan, Y. Liu, S. Peredkov, et al., "Combining Valence-to-Core X-ray Emission and Cu K-edge X-ray Absorption Spectroscopies to Experimentally Assess Oxidation State in Organometallic Cu(I)/(II)/(III) Complexes," *Journal of the American Chemical Society* 144 (2022): 2520–2534, https://doi.org/10.1021/jacs.1c09505.

36. O. O. Fashedemi, H. A. Miller, A. Marchionni, F. Vizza, and K. I. Ozoemena, "Electro-Oxidation of Ethylene Glycol and Glycerol at Palladium-Decorated FeCo@Fe Core–Shell Nanocatalysts for Alkaline Direct Alcohol Fuel Cells: Functionalized MWCNT Supports and Impact on Product Selectivity," *Journal of Materials Chemistry A* 3 (2015): 7145–7156, https://doi.org/10.1039/C5TA00076A.

37. F. L. Huber, S. Amthor, B. Schwarz, B. Mizaikoff, C. Streb, and S. Rau, "Multi-Phase Real-Time Monitoring of Oxygen Evolution Enables in Operando Water Oxidation Catalysis Studies," *Sustainable Energy & Fuels* 2 (2018): 1974–1978, https://doi.org/10.1039/C8SE00328A.

38. T. Wang, Z. Huang, T. Liu, et al., "Transforming Electrocatalytic Biomass Upgrading and Hydrogen Production From Electricity Input to Electricity Output," *Angewandte Chemie* 134 (2022): 202115636, https://doi.org/10.1002/ange.202115636.

39. T. Wang, L. Tao, X. Zhu, et al., "Combined Anodic and Cathodic Hydrogen Production from Aldehyde Oxidation and Hydrogen Evolution Reaction," *Nature Catalysis* 5 (2022): 66–73, https://doi.org/10.1038/s41929-021-00721-y.

40. J. F. Gomes and G. Tremiliosi-Filho, "Spectroscopic Studies of the Glycerol Electro-Oxidation on Polycrystalline Au and Pt Surfaces in Acidic and Alkaline Media," *Electrocatalysis* 2 (2011): 96–105, https://doi.org/10.1007/s12678-011-0039-0.

41. G. Wu, Y. Liu, Y. He, J. Feng, and D. Li, "Reaction Pathway Investigation Using In Situ Fourier Transform Infrared Technique Over Pt/CuO and Pt/TiO2 for Selective Glycerol Oxidation," *Applied Catalysis B: Environmental* 291 (2021): 120061, https://doi.org/10.1016/j.apcatb.2021.120061.

42. Y. Yan, H. Zhou, S.-M. Xu, et al., "Electrocatalytic Upcycling of Biomass and Plastic Wastes to Biodegradable Polymer Monomers and Hydrogen Fuel at High Current Densities," *Journal of the American Chemical Society* 145 (2023): 6144–6155, https://doi.org/10.1021/jacs.2c11861.

43. Y. Holade, C. Morais, K. Servat, T. W. Napporn, and K. B. Kokoh, "Toward the Electrochemical Valorization of Glycerol: Fourier Transform

Infrared Spectroscopic and Chromatographic Studies," *Acs Catalysis* 3 (2013): 2403–2411, https://doi.org/10.1021/cs400559d.

44. Y. Li, X. Wei, R. Pan, et al., "PtAu alloying-modulated hydroxyl and substrate adsorption for glycerol electrooxidation to C 3 products," *Energy & Environmental Science* 17 (2024): 4205–4215, https://doi.org/10.1039/D4EE00485J.

45. X. Han, H. Sheng, C. Yu, et al., "Electrocatalytic Oxidation of Glycerol to Formic Acid by CuCo 2 O 4 Spinel Oxide Nanostructure Catalysts," *Acs Catalysis* 10 (2020): 6741–6752, https://doi.org/10.1021/acscatal.0c01498.

46. X. Yu, E. C. Dos Santos, J. White, et al., "Electrocatalytic Glycerol Oxidation with Concurrent Hydrogen Evolution Utilizing an Efficient MoOx/Pt Catalyst," *Small* 17 (2021): 2104288.

47. Y. Li, X. Wei, L. Chen, J. Shi, and M. He, "Nickel-Molybdenum Nitride Nanoplate Electrocatalysts for Concurrent Electrolytic Hydrogen and Formate Productions," *Nature Communications* 10 (2019): 5335, https://doi.org/10.1038/s41467-019-13375-z.

48. Z. He, J. Hwang, Z. Gong, et al., "Promoting Biomass Electrooxidation Via Modulating Proton and Oxygen Anion Deintercalation in Hydroxide," *Nature Communications* 13 (2022): 3777, https://doi.org/10.1038/s41467-022-31484-0.

49. Z. Ke, N. Williams, X. Yan, et al., "Solar-Assisted Co-Electrolysis of Glycerol and Water for Concurrent Production of Formic Acid and Hydrogen," *Journal of Materials Chemistry A* 9 (2021): 19975–19983, https://doi.org/10.1039/D1TA02654B.

50. S. Wang, Y. Yan, Y. Du, et al., "Inhibiting the Deep Reconstruction of Ni-Based Interface by Coordination of Chalcogen Anions for Efficient and Stable Glycerol Electrooxidation," *Advanced Functional Materials* 34 (2024): 2404290, https://doi.org/10.1002/adfm.202404290.

51. L. Ma, Y. Miao, J. Yang, et al., "Promoting Electrocatalytic Glycerol C—C Bond Cleavage to Formate Coupled With H 2 Production Over a Cu x Ni 2–x P Catalyst," *Advanced Energy Materials* 14 (2024): 2401061, https://doi.org/10.1002/aenm.202401061.

52. Z. Chen, C. Liu, X. Zhao, et al., "Promoted Glycerol Oxidation Reaction in an Interface-Confined Hierarchically Structured Catalyst," *Advanced Materials* 31 (2019): 1804763, https://doi.org/10.1002/adma.201804763.

53. W. Luo, H. Tian, Q. Li, et al., "Controllable Electron Distribution Reconstruction of Spinel NiCo 2 O 4 Boosting Glycerol Oxidation at Elevated Current Density," *Advanced Functional Materials* 34 (2024): 2306995, https://doi.org/10.1002/adfm.202306995.

54. Y. Zhou, Y. Shen, and J. Xi, "Seed-Mediated Synthesis of PtxAuy@Ag Electrocatalysts for the Selective Oxidation of Glycerol," *Applied Catalysis B: Environmental* 245 (2019): 604–612, https://doi.org/10.1016/j.apcatb.2019.01.009.

55. D. Kim, C. Dang Van, M. S. Lee, M. Kim, M. H. Lee, and J. Oh, "Selective Formic Acid Production in Ni and NiFe Layered Hydroxides via Glycerol Electro-Oxidation," *ACS Catalysis* 14 (2024): 7717–7725, https://doi.org/10.1021/acscatal.4c01250.

56. D. Kim, L. S. Oh, Y. C. Tan, H. Song, H. J. Kim, and J. Oh, "Enhancing Glycerol Conversion and Selectivity Toward Glycolic Acid via Precise Nanostructuring of Electrocatalysts," *ACS Catalysis* 11 (2021): 14926–14931, https://doi.org/10.1021/acscatal.1c04581.

57. Z. Zhao, X. Shen, X. Luo, et al., "Electric Field Redistribution Triggered Surface Adsorption and Mass Transfer to Boost Electrocatalytic Glycerol Upgrading Coupled With Hydrogen Evolution," *Advanced Energy Materials* 14 (2024): 2400851, https://doi.org/10.1002/aenm.202400851.

58. W. Chen, L. Zhang, L. Xu, et al., "Pulse potential mediated selectivity for the electrocatalytic oxidation of glycerol to glyceric acid," *Nature Communications* 15 (2024): 2420, https://doi.org/10.1038/s41467-024-46752-4.

Supporting Information

Additional supporting information can be found online in the Supporting Information section.

Supporting File: aenm70621-supp-0001-SupMat.pdf